

See discussions, stats, and author profiles for this publication at: <https://www.researchgate.net/publication/263955443>

# Hybrid Au–Fe<sub>3</sub>O<sub>4</sub> Nanoparticles: Plasmonic, Surface Enhanced Raman Scattering, and Phase Transition Properties

ARTICLE in THE JOURNAL OF PHYSICAL CHEMISTRY C · JULY 2013

Impact Factor: 4.77 · DOI: 10.1021/jp4040826

---

CITATIONS

14

---

READS

97

## 5 AUTHORS, INCLUDING:



[Adnen Mlayah](#)

Paul Sabatier University - Toulouse III

106 PUBLICATIONS 1,427 CITATIONS

[SEE PROFILE](#)



[Noureddine Jouini](#)

Université Paris 13 Nord

96 PUBLICATIONS 1,619 CITATIONS

[SEE PROFILE](#)



[Leila Samia Smiri](#)

University of Carthage

94 PUBLICATIONS 805 CITATIONS

[SEE PROFILE](#)

# Hybrid Au–Fe<sub>3</sub>O<sub>4</sub> Nanoparticles: Plasmonic, Surface Enhanced Raman Scattering, and Phase Transition Properties

Amine Mezni,<sup>†,‡</sup> Imen Balti,<sup>†,§</sup> Adnen Mlayah,<sup>\*,‡</sup> Noureddine Jouini,<sup>§</sup> and Leila Samia Smiri<sup>†</sup>

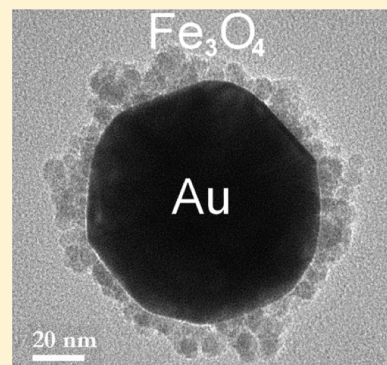
<sup>†</sup>Unité de recherche "Synthèse et Structure de Nanomatériaux" UR11ES30, Faculté des Sciences de Bizerte, Université de Carthage, 7021 Jarzouna, Tunisia

<sup>‡</sup>Centre d'Elaboration de Matériaux et d'Etudes Structurales, CNRS, UPR 8011, Université de Toulouse, 29 Rue Jeanne Marvig, 31055 Toulouse, France

<sup>\*</sup>Laboratoire des Sciences des Procédés et Matériaux, LSPM, CNRS, UPR 3407 Université Paris XIII, 99 Avenue J. B. Clément, 93430 Villetteuse, France

## Supporting Information

**ABSTRACT:** In this work, we report on the synthesis of hybrid Au–Fe<sub>3</sub>O<sub>4</sub> nanoparticles (NPs) using a novel one-pot synthesis method that makes use of triethylene glycol as a solvent, a reducing agent, and a stabilizing layer. The produced nanoparticles consist of Au cores decorated with magnetite Fe<sub>3</sub>O<sub>4</sub> nanoparticles. Optical absorption measurements combined with numerical simulations showed that the Au–Fe<sub>3</sub>O<sub>4</sub> nanoparticles exhibit a localized surface plasmon resonance clearly red-shifted with respect to that of bare Au nanoparticles. This strong plasmonic resonance is exploited to produce surface-enhanced Raman scattering (SERS) from both the organic molecules and the iron oxide surrounding the Au cores. We found that the SERS signal exhibits strong temporal fluctuations which are used to identify the origin of the observed Raman lines. In particular, we clearly point out the presence of an iron hydroxide ( $\gamma$ -FeOOH) layer at the surface of the Fe<sub>3</sub>O<sub>4</sub> nanoparticles forming the shell. This result is supported by numerical simulations of the plasmonic near field generated by the Raman probe. Moreover, we investigate the light-induced phase transition from magnetite to hematite ( $\alpha$ -Fe<sub>2</sub>O<sub>3</sub>). Owing to the strong SERS effect we were able to detect the formation of diiron-oxo bonds during the phase transition. These bonds are ascribed to the presence of a mixed magnetite/maghemite phase. We thus propose a new scheme where the phase transition is triggered by the iron hydroxide surface layer. Such a transition is here studied for the first time in Au–Fe<sub>3</sub>O<sub>4</sub> hybrid nanoparticles where the gold cores act as plasmonic nanoheaters responsible for the thermally induced phase transition.



## 1. INTRODUCTION

The ability to integrate multiple functions into a single composite nanoparticle with tunable composition, size, and morphology is a promising strategy for achieving novel properties with applications in diverse areas such as multimodal biological detection,<sup>1</sup> catalysis,<sup>2</sup> solar energy conversion,<sup>3,4</sup> and optoelectronic applications.<sup>5</sup> In recent years, significant advances in the controlled synthesis of composite nanoparticles have been made.<sup>6</sup> The general approach is first to prepare nanoparticles of one material and then to use them as nucleation seeds to grow additional materials. However, only a few hybrid nanoparticles show a reasonable level of control over particle size distribution and homogeneity.<sup>7,8</sup>

Among these hybrid nanomaterials, Au–Fe<sub>3</sub>O<sub>4</sub> bifunctional<sup>9</sup> nanoparticles exhibiting magneto-optical properties<sup>8,10,11</sup> have attracted increasing interest for their applications in magnetic resonance,<sup>10</sup> magneto-motive imaging,<sup>12</sup> bioseparation and pathogen detection,<sup>13,14</sup> drug delivery,<sup>15</sup> and biosensing.<sup>16</sup>

The main difficulty in preparing such particles lies in the weak interaction between iron oxide (e.g.,  $\alpha$ -Fe<sub>2</sub>O<sub>3</sub> and Fe<sub>3</sub>O<sub>4</sub>) and metal (e.g., Au, Ag, Pt, and Pd) nanoparticles. The key to form Au–Fe<sub>3</sub>O<sub>4</sub> nanoparticles is to suppress the homogeneous

nucleation and to promote the heterogeneous growth of Fe<sub>3</sub>O<sub>4</sub> on Au seeds. To date, the most promising method is based on a thermal decomposition approach in the presence of capping molecules.<sup>17–19</sup> In brief, Au seeds are formed and dispersed in an organic solvent first. The Fe precursor is then injected and decomposed at high temperature. Eventually Fe<sub>3</sub>O<sub>4</sub> nanoparticles nucleate and grow epitaxially on the Au seeds. However, the capping ligands at the surface of the preformed seeds could affect the ability of iron oxide to , Au–Fe<sub>3</sub>O<sub>4</sub> nanoparticles with well-defined dimform on the seed's surface. Recently, dumbbell-like structure were synthesized<sup>19</sup> using the thermal decomposition method. Another approach, reported by Jie Bao et al.,<sup>20</sup> consists of synthesizing Au and Fe<sub>3</sub>O<sub>4</sub> nanoparticles separately and then linking them by appropriate chemical bond linkage. Also dumbbell-like Au–Fe<sub>3</sub>O<sub>4</sub> nanoparticles (NPs) were synthesized using the competitive growth of Au<sub>2</sub> on preformed Au<sub>1</sub>–Fe<sub>3</sub>O<sub>4</sub> NPs.<sup>21</sup> In a recent work, HongLing Liu et al.<sup>22</sup> have used a two-step nanoemulsion process to

Received: April 25, 2013

Revised: July 5, 2013

Published: July 11, 2013



synthesize Au–Fe<sub>3</sub>O<sub>4</sub> hybrid core–shell nanoparticles in one pot, using nontoxic precursors. They found that the structural arrangement enhances the magnetic and optical functionalities beyond those of the individual components.

In this work, we report on the synthesis of Fe<sub>3</sub>O<sub>4</sub>-decorated AuNPs formed in one pot in triethylene glycol. The latter is acting as a solvent, a reducing agent, and a capping/stabilizing layer. This simple polyol-assisted method demonstrates the preparation of Fe<sub>3</sub>O<sub>4</sub>-decorated AuNPs without addition of any templates or complex metal ligands. The plasmonic properties of the synthesized Fe<sub>3</sub>O<sub>4</sub>-decorated AuNPs are investigated using optical absorption measurements combined with numerical simulations. We also exploit the strong localization of the surface plasmon field in the Fe<sub>3</sub>O<sub>4</sub> shell to produce surface-enhanced Raman scattering (SERS). The latter is used to gain information not only on the organic molecules surrounding the nanoparticle but also on the nanoparticle structure itself. Owing to a detailed analysis of the SERS signal, and its temporal fluctuations, we were able to detect the presence of an iron hydroxide (lepidocrocite,  $\gamma$ -FeOOH) layer that plays an important role in the laser-induced transition of the iron oxide shell from the magnetite (Fe<sub>3</sub>O<sub>4</sub>) phase to the hematite ( $\alpha$ -Fe<sub>2</sub>O<sub>3</sub>) phase. This phase transition has been the subject of several published works;<sup>23–25</sup> all of them were performed either on thin magnetite films or on pure magnetite nanoparticles. Here, we use the plasmonic hyperthermia effect to induce such a phase transition for the first time in hybrid Au–Fe<sub>3</sub>O<sub>4</sub> nanoparticles.

## 2. EXPERIMENTAL SECTION

### 2.1. Synthesis of Au–Fe<sub>3</sub>O<sub>4</sub> Decorated Nanoparticles.

The preparation of Fe<sub>3</sub>O<sub>4</sub>-decorated AuNPs involved an initial synthesis of Au nanoparticles by thermal reduction of the Au precursor and thermal decomposition of Fe(acac)<sub>3</sub> onto the surface of the preformed Au nanoparticles at high temperature. A typical synthesis was carried out in a 100 mL three-neck round-bottomed flask equipped with condenser, mechanical stirrer, and thermograph, mixing 0.038 mmol of HAuCl<sub>4</sub>·3H<sub>2</sub>O (purchased from Aldrich) with 0.17 mmol of iron(III) acetylacetone (Fe(acac)<sub>3</sub>, 99% Acros) in 50 mL of triethylene glycol (TREG) (ACROS Organics, 98%) with vigorous stirring. The reaction mixture was first slowly heated to 180 °C and kept at that temperature for 30 min, then quickly heated to reflux (~280 °C) and kept at reflux for another 30 min. After cooling to room temperature, a brown homogeneous colloidal suspension containing Fe<sub>3</sub>O<sub>4</sub>-decorated AuNPs was obtained. The product was separated by centrifugation, washed several times with ethanol/acetone (2:1), and redispersed in ethanol. After centrifugation, the products were deposited on the bottom of the tubes, and the supernatant solution became clear and colorless, indicating that no Au nanoparticles are present in the solution.

### 2.2. Structural and Morphological Characterization.

The morphology of the Fe<sub>3</sub>O<sub>4</sub>-decorated AuNPs was characterized by transmission electron microscopy (TEM) using a JEOL-JFC 1600 microscope operating at an accelerating voltage of 100 keV. The chemical composition of the Fe<sub>3</sub>O<sub>4</sub>-decorated AuNPs was determined by energy-dispersive X-ray spectroscopy (EDX) attached to the TEM.

**2.3. Optical Characterization.** The optical extinction spectra of Au and Au–Fe<sub>3</sub>O<sub>4</sub> nanoparticles dispersed in ethanol were acquired using a Perkin-Elmer Lambda 11 UV-vis spectrophotometer. The Raman experiments were carried out

using a Jobin-Yvon XploRa setup. The excitation laser beam was focused onto the sample through the 100X objective of a confocal microscope. The laser spot size was diffraction limited to 355 nm at the 638 nm excitation wavelength. For the laser-induced phase transition experiments, the laser power was varied from 0.014 to 14 mW which corresponds to laser intensities from  $1.4 \times 10^4$  to  $1.4 \times 10^7$  W cm<sup>-2</sup>. For the SERS blinking experiments, the time evolution of the Raman spectra has been recorded with a time step of 0.5 s and an accumulation time of 0.5 s.

**2.4. DDA Simulations.** Simulations of the optical extinction spectra were performed using the discrete dipole approximation (DDA) implemented in DDSCAT 7.2.2 software.<sup>26,27</sup> The wavelength-dependent refractive indices of gold and bulk magnetite Fe<sub>3</sub>O<sub>4</sub> were taken from Johnson and Christy<sup>28</sup> and Schlegel et al.,<sup>29</sup> respectively. The interdipole distance was kept as small as 0.8 nm to ensure full convergence of the calculations.

## 3. RESULTS AND DISCUSSION

**3.1. Synthesis and Characterization of Fe<sub>3</sub>O<sub>4</sub>-Decorated AuNPs.** The synthesis of the Fe<sub>3</sub>O<sub>4</sub>-decorated AuNPs was achieved by controlled sequential reactions in a one-pot chemical process, where gold salt HAuCl<sub>4</sub> and iron(III) acetylacetone are mixed together in triethylene glycol. As shown by transmission electron microscopy (Figure 1a) and

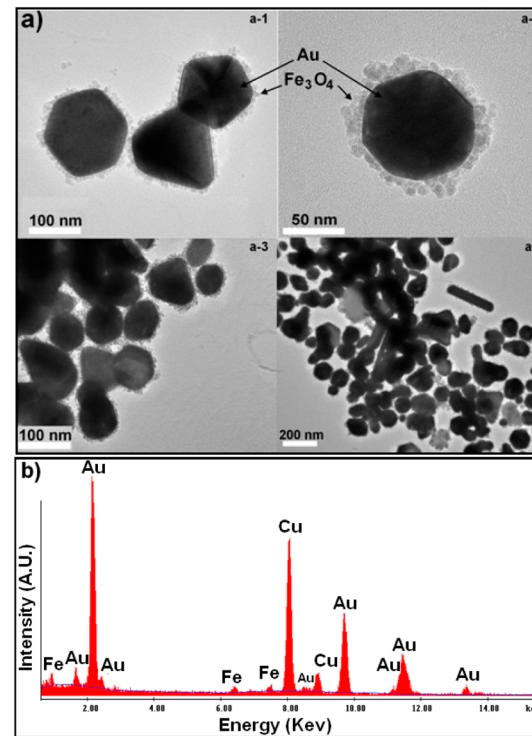


**Figure 1.** Characterization of Fe<sub>3</sub>O<sub>4</sub>-decorated AuNPs using transmission electron microscopy (a) and energy dispersive X-ray spectroscopy (b). For the majority of the nanoparticles, the Au core is quasi-spherical with an average size of 90 nm (a-1, a-2); however, hexagonal, triangular, and elongated Au cores ranging from 80 to 150 nm are also found (a-3, a-4). The shell surrounding the Au cores is formed by a compact arrangement of iron oxide NPs with a size around 7 nm. Fe, Au, and Cu are present in the EDX spectrum (b). The presence of Cu is due to the copper grid used for the TEM/EDX experiments.

energy dispersive X-ray (EDX) spectroscopy (Figure 1b), the final products consist mainly of faceted quasi-spherical gold cores (around 90 nm) surrounded by close-packed iron oxide NPs (around 7 nm) forming a decoration (Figure 1a-1, a-2). Triangular, hexagonal, and elongated Au cores are also present (Figure 1a-3, a-4).

The formation of Au–Fe<sub>3</sub>O<sub>4</sub> nanoparticles is based on an initial production of the Au nanoparticles followed by a hydroxylation-condensation process, of an intermediate iron alkoxy-salt complex, onto the surface of the preformed Au nanoparticles. The proposed chemical reaction mechanism is described in Figure 2.

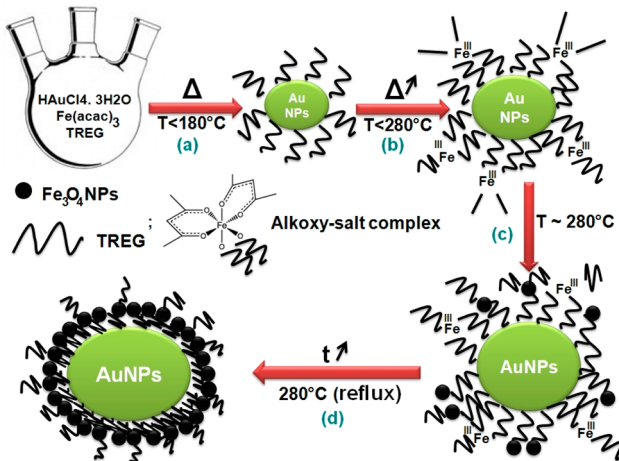


**Figure 2.** Schematic illustration of Fe<sub>3</sub>O<sub>4</sub>-decorated AuNP synthesis. Formation of AuNPs in the polyol solvent (a), decomposition of the iron(III) precursor at the surface of the preformed AuNPs and formation of an intermediate iron alkoxy-salt complex (b), nucleation of Fe<sub>3</sub>O<sub>4</sub> seeds (c), and growth of Fe<sub>3</sub>O<sub>4</sub> at the AuNP surface leading to Fe<sub>3</sub>O<sub>4</sub>-decorated AuNPs (d).

First, Au nanoparticles are formed around 180 °C and are stabilized by triethylene glycol molecules grafted to the Au surface via electrostatic bonds. Second, as the temperature increases, the iron(III) acetylacetone starts to decompose at the reactive surface of the AuNPs and forms an intermediate iron alkoxy-salt complex between the iron salt and the triethylene glycol.<sup>30</sup> We suggest that the formation of an intermediated iron alkoxy-salt complex at the surface of the AuNPs slows down the growth of the AuNPs and prevents their agglomeration at high temperature. Moreover, the iron alkoxy-salt complex at the surface of the AuNPs acts as a nucleation site for the growth of iron oxide NPs via inorganic polymerization reactions<sup>31</sup> which are also catalyzed by the high reactivity of the Au surface (Figure 2).

The nucleation of the iron oxide starts below the boiling temperature of triethylene glycol (280 °C). Indeed, it was observed that the solution becomes dark brown at 260 °C with some turbidity. Under these conditions, it is expected that nucleation events are sluggish, and the number of nuclei is small. At 280 °C, further nucleation and growth of the iron oxide complex take place. Because heterogeneous nucleation is preferred over homogeneous nucleation,<sup>32</sup> iron ions tend to condense on pre-existing iron oxide seeds present at the surface of AuNPs, rather than forming new nuclei in the solution.

To test the validity of the proposed reaction mechanism, we conducted the same synthesis protocol but in the presence of

excess of sodium citrate. Sodium citrate has a strong affinity toward gold<sup>33</sup> and is therefore expected to completely coat the gold nanoparticles thus preventing the initial hydroxylation-condensation of the iron alkoxy-salt complex at the Au surface. With addition of sodium citrate we did not obtain Fe<sub>3</sub>O<sub>4</sub>-decorated AuNPs. Instead, we obtained large gold aggregates with small iron oxide NPs adsorbed on their surface. This corroborates the need for the initial crucial step that involves the formation of the iron alkoxy-salt complex at the Au surface and subsequently triggers the hydroxylation-condensation process to form iron oxide NPs (see discussion in Supporting Information).

It is difficult to identify the magnetite iron oxide phase based on XRD data due to the similar lattice characteristics of the iron atoms in magnetite Fe<sub>3</sub>O<sub>4</sub> and maghemite γ-Fe<sub>2</sub>O<sub>3</sub>. Notice that X-ray diffraction showed no signature of the iron oxide NPs because of their very small overall volume compared to that of the Au cores. Since different iron oxide phases have distinct characteristic bond vibrations, they can be readily identified using Raman scattering. Owing to SERS experiments, we found that the NPs forming the decoration around the Au cores consist of magnetite Fe<sub>3</sub>O<sub>4</sub> NPs. We have also detected the presence of lepidocrocite (γ-FeOOH) as will be shown later.

**3.2. Plasmonic Properties.** The measured optical extinction spectra of the Fe<sub>3</sub>O<sub>4</sub>-decorated AuNPs are shown in Figure 3B. The spectrum of 90 nm spherical bare gold NPs is

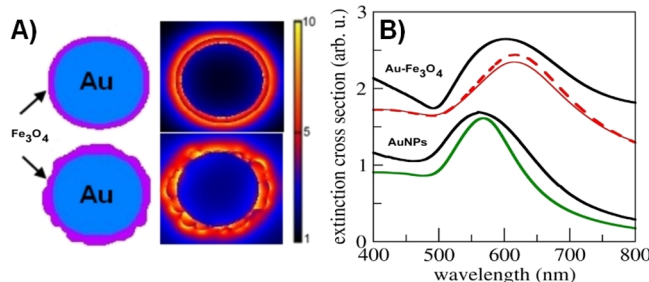


**Figure 3.** Plasmonic response of bare Au and Au–Fe<sub>3</sub>O<sub>4</sub> nanoparticles dispersed in ethanol. Measured absorbance spectra of the bare AuNPs and Fe<sub>3</sub>O<sub>4</sub>-decorated AuNPs peaking at 563 and 603 nm (black lines), respectively. DDA simulated extinction spectra of bare AuNPs (green line) and Au–Fe<sub>3</sub>O<sub>4</sub> NPs (red lines) with a smooth (continuous line) and rough shell (dashed line). The upper part of the figure shows the distribution of the plasmonic near-field intensity  $|E/E_0|^2$  for the Au–Fe<sub>3</sub>O<sub>4</sub> nanoparticles with a smooth and a rough Fe<sub>3</sub>O<sub>4</sub> shell. The excitation wavelength is 616 nm in both cases, and the incident electric field is circularly polarized.

also shown for comparison. In Figure 3B are also displayed the spectra simulated using the discrete dipole approximation (DDA) method.<sup>26</sup> Two models were considered: (i) the Au core is surrounded by a smooth regular shell with a constant thickness of 7 nm (i.e., a perfect core–shell structure); (ii) the Au core is surrounded by a rough irregular shell generated using a random distribution of hemispherical surface particles with sizes between 3 and 10 nm, representing the iron oxide NP decoration. In both models, the iron oxide volume is the same. Model (ii) mimics the actual shell structure as observed in Figure 2. We assume that the iron oxide forming the shell corresponds to the magnetite phase Fe<sub>3</sub>O<sub>4</sub>. In the simulations, the medium surrounding the NPs is ethanol as in experiments.

First, the extinction spectrum of the Fe<sub>3</sub>O<sub>4</sub>-decorated AuNPs clearly shows a surface plasmon resonance peaking around 603

nm, red-shifted by more than 40 nm with respect to the surface plasmon resonance of the bare AuNPs. This red shift is well-known<sup>34</sup> and is due to the increase of the optical index of the medium surrounding the gold. Indeed, the optical index of (bulk)  $\text{Fe}_3\text{O}_4$  is around 2.35 (at 600 nm) and is much larger than that of ethanol (1.36). This red shift is confirmed by the DDA simulations; the spectra calculated for the bare AuNPs and for the regular Au– $\text{Fe}_3\text{O}_4$  core–shell NPs are in satisfactory agreement with the measured ones, thus corroborating the nature of the iron oxide NPs (magnetite  $\text{Fe}_3\text{O}_4$ ). However, the surface plasmon resonances in the measured spectra are broader than those in the simulated spectra certainly because of the inhomogeneous broadening due to size and shape fluctuations of the Au cores. Moreover, the irregular shape of the  $\text{Fe}_3\text{O}_4$  decoration may also impact the plasmonic resonance. The spectra simulated with either a smooth or a rough  $\text{Fe}_3\text{O}_4$  shell show that this is not the case. Indeed, both spectra are very similar, and the increase of the resonance line width due to the  $\text{Fe}_3\text{O}_4$  shell roughness is very weak. In fact, the inhomogeneous contribution to the resonance line width due to the shell roughness is smaller than the homogeneous contribution which is mainly due to the optical absorption into the  $\text{Fe}_3\text{O}_4$  (and in the Au core). As a matter fact, the imaginary part of the optical index of bulk  $\text{Fe}_3\text{O}_4$  is around 0.6 (at 600 nm) and is responsible for the broadening of the plasmonic resonance (compared to that of bare gold nanoparticles).

To fully understand the plasmonic properties of the  $\text{Fe}_3\text{O}_4$ -decorated AuNPs we have plotted in Figure 3A the near-field maps<sup>35</sup> associated with the plasmonic resonances of the smooth and of the rough Au– $\text{Fe}_3\text{O}_4$  nanoparticle models. It is interesting to notice that in both particles the field intensity is maximum at the Au– $\text{Fe}_3\text{O}_4$  interface but also at the  $\text{Fe}_3\text{O}_4$  surface. As checked by simulations, this effect is due to the rather small  $\text{Fe}_3\text{O}_4$  shell thickness (around 7 nm) that allows polarization charges to be generated at the  $\text{Fe}_3\text{O}_4$  surface. For large  $\text{Fe}_3\text{O}_4$  shell thickness (around 20 nm) one recovers a maximum of field intensity only at the Au– $\text{Fe}_3\text{O}_4$  interface, as expected for a gold nanoparticle embedded in an infinite  $\text{Fe}_3\text{O}_4$  matrix. This point is particularly important for the interpretation of the SERS data as will be discussed now.

**3.3. SERS Properties.** To analyze the structure and chemical composition of the iron oxide shell surrounding the Au cores, we have performed Raman scattering experiments using resonant excitation of the surface plasmons of the  $\text{Fe}_3\text{O}_4$ -decorated AuNPs (Figure 4). The  $\text{Fe}_3\text{O}_4$ -decorated AuNPs were drop casted on a glass substrate and thus formed aggregates from which the Raman signal was recorded. During the experiments we have observed strong fluctuations of the Raman scattering intensities as shown in the inset of Figure 4 (see movie in Supporting Information). This phenomenon is known as SERS blinking<sup>36</sup> and is typical of Raman scattering by a small number of molecules located at plasmonic hot spots.<sup>37–39</sup> Due to their thermally activated motion and rotation, the molecules may change conformation thus exploring different elements of the Raman tensor associated to each vibration mode. In our case, the NPs are stabilized by triethylene glycol, and all Raman features observed in the range 750–1750 cm<sup>−1</sup> (Figure 4) are due to stretching, twisting, and wagging of  $\text{CH}_2$  and C–OH groups of triethylene glycol (see table in Supporting Information). The snapshot spectra in Figure 4 show that some Raman features are absent at given instants but may become very intense (several thousand of counts/s) at others. However, this SERS blinking is not

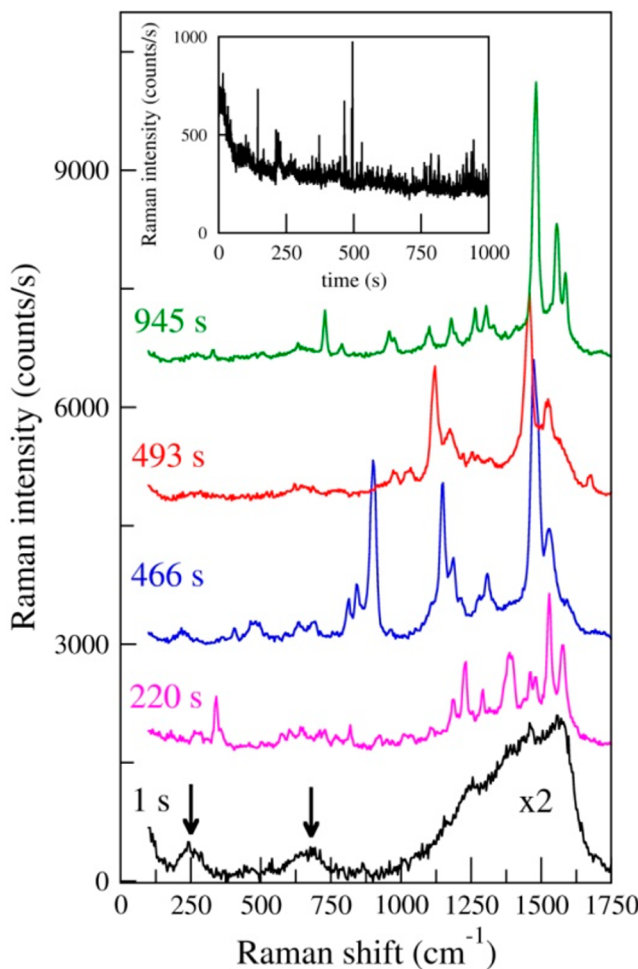


**Figure 4.** SERS spectra at selected instants. The excitation wavelength 638 nm is resonant with the plasmonic absorption of the Au– $\text{Fe}_3\text{O}_4$  nanoparticles. The inset shows the temporal evolution of the SERS signal integrated over the whole spectral range. The arrows indicate the bands ascribed to magnetite  $\text{Fe}_3\text{O}_4$  (670 cm<sup>−1</sup>) and lepidocrocite  $\gamma\text{-FeOOH}$  (250 cm<sup>−1</sup>).

observed for all Raman features. Indeed, two Raman bands located at 250 and 670 cm<sup>−1</sup> do not exhibit blinking (see movie in Supporting Information) and can therefore be clearly distinguished from the contribution of triethylene glycol vibration modes. The relative intensities of these two bands may change from an aggregate to the other, but the general trends are the same: they do not exhibit blinking contrary to the Raman features of triethylene glycol. We therefore attribute these two bands to the iron oxide NPs surrounding the Au cores. According to the well-documented Raman studies of iron oxide phases and hydroxides,<sup>40–43</sup> the 670 cm<sup>−1</sup> Raman band can be unambiguously attributed to the  $\text{A}_{1g}$  vibration mode of magnetite  $\text{Fe}_3\text{O}_4$ .<sup>42</sup> However, the 250 cm<sup>−1</sup> Raman band cannot be assigned to any of the iron oxide phases. On the other hand, the 250 cm<sup>−1</sup> feature is dominant in the Raman spectra of lepidocrocite<sup>43</sup> which is an iron hydroxide with an orthorhombic crystal structure:  $\gamma\text{-FeOOH}$  is a common product of iron oxidation.

The SERS experiments confirm that the NPs surrounding the Au cores are magnetite  $\text{Fe}_3\text{O}_4$  NPs, and they also reveal the presence of lepidocrocite  $\gamma\text{-FeOOH}$ . Lepidocrocite arises from iron oxidation due to exposure of the nanoparticles to air and may thus form 1 or 2 nm thick capping layer at the surface of

the  $\text{Fe}_3\text{O}_4$  shell. Lepidocrocite could not be detected in the Raman spectra of pure  $\text{Fe}_3\text{O}_4$  nanoparticles certainly because of its small scattering volume. In our  $\text{Fe}_3\text{O}_4$ -decorated AuNPs it was possible to detect lepidocrocite owing to the plasmonic resonance carried by the Au core. Moreover, as shown in Figure 3, the plasmonic near-field intensity is maximum at the surface of the  $\text{Fe}_3\text{O}_4$  shell which further enhances the Raman scattering from this region.

The presence of lepidocrocite could play an important role in the phase transition properties of the Au– $\text{Fe}_3\text{O}_4$  NPs. To further confirm the presence of a lepidocrocite layer at the surface of the  $\text{Fe}_3\text{O}_4$  shell, we have investigated the dependence of the SERS signal on excitation wavelength.

Figure 5B shows the time-averaged Raman spectra excited at 532, 638, and 785 nm. As expected, the overall SERS intensity

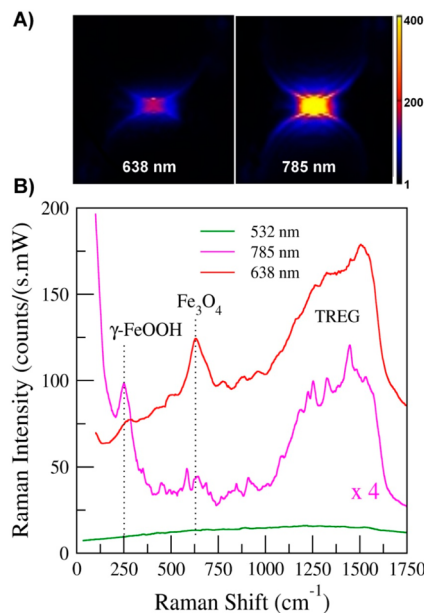


**Figure 5.** SERS signal dependence on excitation wavelength. The spectra were averaged over a three minutes accumulation time. The spectrum excited at 785 nm has been magnified ( $\times 4$ ). Dotted lines indicate the frequencies of the magnetite  $\text{Fe}_3\text{O}_4$  and lepidocrocite bands  $\gamma\text{-FeOOH}$ . The upper part of the figure shows the maps of the plasmonic near-field intensity  $|E/E_0|^2$  excited at 638 and 785 nm for a Au– $\text{Fe}_3\text{O}_4$  dimer with an edge-to-edge separation between the Au cores of 8 nm (the corresponding optical extinction spectrum is given in the Supporting Information). The incident light is circularly polarized to excite both transverse and longitudinal surface plasmons.

is maximum for excitation at 638 nm, i.e., close to the LSPR of the Au– $\text{Fe}_3\text{O}_4$  NPs (Figure 3B). Moreover, the spectra in Figure 5B were recorded from an aggregate where the  $250\text{ cm}^{-1}$  Raman feature associated with lepidocrocite is hardly seen for excitation at 638 nm. However, it clearly comes out for excitation at 785 nm.

It is well-known that the near-field electromagnetic interaction between metal nanoparticles leads to plasmonic hot spots located inside the gap regions between the nanoparticles.<sup>44,45</sup> The wavelength of the corresponding resonances are red-shifted with respect to the LSPR of isolated particles, the red shift being directly connected to the gap width.<sup>45</sup> Such plasmonic gap modes are likely to occur in aggregates of  $\text{Fe}_3\text{O}_4$ -decorated AuNPs. The  $\text{Fe}_3\text{O}_4$  decoration (which is 7 nm thick in average) and the stabilizing molecules

(triethylene glycol chain is around 2 nm long) impose an average minimum spacing of 18 nm between the Au cores. However, as shown in Figure 1a, the shell thickness is not regular, and the separation between the Au cores may be smaller than 18 nm leading to strongly red-shifted plasmonic response. To investigate the influence of plasmonic gap modes on the intensities of the magnetite and lepidocrocite Raman features (Figure 5B), we have simulated the optical extinction spectra (see Supporting Information) and plasmonic near fields (Figure 5A) of two interacting  $\text{Fe}_3\text{O}_4$ -decorated AuNPs forming a dimer. The separation between the Au cores is 8 nm, and the  $\text{Fe}_3\text{O}_4$  shells were generated with a roughness similar to that shown in Figure 3A.

As can be seen in Figure 5A, for excitation at 638 and 785 nm, the plasmonic near field is strongly localized inside the  $\text{Fe}_3\text{O}_4$  gap between the Au cores. Therefore, the Raman scattering from the surface region of  $\text{Fe}_3\text{O}_4$  is strongly enhanced, and the presence of a lepidocrocite surface layer can be detected. Moreover, the plasmonic field intensity excited at 785 nm is larger than that generated at 638 nm. Using the spatial integral of the near-field intensity maps, shown in Figure 5A, we can estimate the plasmonic intensity ratio  $I_{785}/I_{638} = 2.55$ . This explains why the SERS signal of lepidocrocite is better seen with excitation at 785 nm (Figure 5B), hence confirming the presence of lepidocrocite at the surface of the  $\text{Fe}_3\text{O}_4$  shell.

**3.4. Phase Transition Properties.** The transformation of magnetite ( $\text{Fe}_3\text{O}_4$ ) into hematite ( $\alpha\text{-Fe}_2\text{O}_3$ ) caused by laser heating is well-known<sup>23</sup> and has been investigated using Raman spectroscopy.<sup>22,23,33</sup> On the basis of the temperature dependence of the Stokes/anti-Stokes Raman intensity ratio, and of the vibration frequencies, Shebanova et al.<sup>41</sup> showed that the phase transition in natural magnetite starts at  $240\text{ }^\circ\text{C}$ . Our  $\text{Fe}_3\text{O}_4$ -decorated AuNPs efficiently absorb light at their plasmonic resonance (Figure 3B). The stored electromagnetic energy is then converted into heat and released to the surrounding medium via electron plasmons, electron–electron, and electron–phonons interactions.<sup>46</sup> The Au core acts as a heat nanosource that may raise the temperature in the  $\text{Fe}_3\text{O}_4$  shell thus leading to a phase transition. To investigate this plasmonic-assisted phase transition process, we have performed SERS experiments with variable laser intensity.

As shown in Figure 6, for laser intensity below  $1.4 \times 10^5\text{ W cm}^{-2}$  the Raman features characteristic of lepidocrocite and magnetite and of the triethylene glycol are clearly observed. With laser intensity increasing to  $1.4 \times 10^6\text{ W cm}^{-2}$ , Raman bands at  $350$ ,  $500$ , and  $720\text{ cm}^{-1}$  characteristic of, respectively, the  $T_1$ ,  $E$ , and  $A_1$  vibration modes of maghemite ( $\gamma\text{-Fe}_2\text{O}_3$ ) clearly appear.<sup>23</sup> In addition, a strong peak is now visible around  $870\text{ cm}^{-1}$ . This peak is not found in any of the natural iron oxide<sup>41</sup> or hydroxide phases.<sup>40</sup> At  $3.5 \times 10^6\text{ W cm}^{-2}$ , the Raman features characteristic of hematite  $\alpha\text{-Fe}_2\text{O}_3$  come out; their intensity clearly increases at  $7 \times 10^6\text{ W cm}^{-2}$  and becomes dominant at  $1.4 \times 10^7\text{ W cm}^{-2}$ . At the same time the Raman bands of maghemite  $\gamma\text{-Fe}_2\text{O}_3$  disappear as well as the peak at  $870\text{ cm}^{-1}$ .

It has been already reported that pure fine  $\text{Fe}_3\text{O}_4$  particles yield maghemite  $\gamma\text{-Fe}_2\text{O}_3$  with increasing temperature,<sup>23–25</sup> whereas in large particles there is a disproportionation of  $\alpha\text{-Fe}_2\text{O}_3$  and  $\text{Fe}_3\text{O}_4$  from  $\text{Fe}_{3-x}\text{O}_4$  and the proportion of hematite increases with temperature. This size-dependent behavior was attributed to oxidation-induced lattice strain<sup>47</sup> and is in agreement with our observations: in our 7 nm  $\text{Fe}_3\text{O}_4$  NPs we

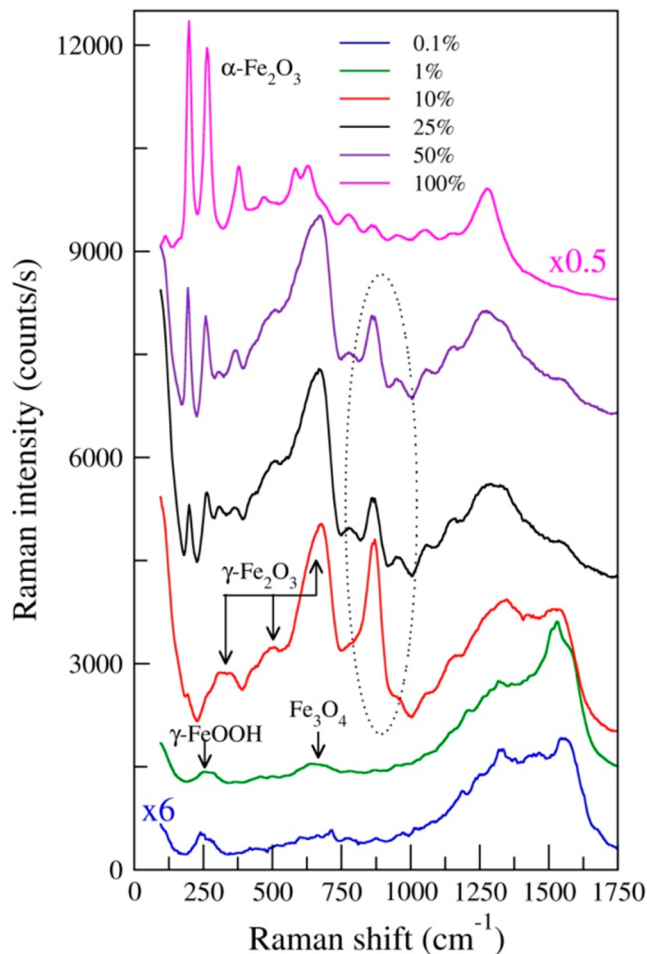


**Figure 6.** Phase transition properties of the  $\text{Fe}_3\text{O}_4$ -decorated AuNPs revealed by SERS spectra excited at 638 nm with laser intensity ranging from  $1.4 \times 10^4 \text{ W cm}^{-2}$  (0.1% of the maximum intensity) to  $1.4 \times 10^7 \text{ W cm}^{-2}$  (100% of the maximum intensity). The spectra are time-averaged. The arrows indicate the bands associated with lepidocrocite, magnetite, and maghemite. All Raman features in the spectrum obtained at  $1.4 \times 10^7 \text{ W cm}^{-2}$  (100%) are due to the phonons of hematite  $\alpha\text{-Fe}_2\text{O}_3$ . The transient peak at  $870 \text{ cm}^{-1}$  ascribed to oxo-bridge di-iron bonds is highlighted in the figure.

observe the transition from magnetite to hematite with an intermediate maghemite phase. Moreover, the peak at  $870 \text{ cm}^{-1}$  is also associated with the intermediate maghemite state. According to Kurtz,<sup>48</sup> oxo-bridge di-iron  $\text{Fe}-\text{O}-\text{Fe}$  has a characteristic intense Raman active vibration mode around  $870 \text{ cm}^{-1}$ . Such  $\text{Fe}-\text{O}-\text{Fe}$  bonds are expected at the interface between the magnetite and the maghemite phases of iron oxide since  $\text{Fe}_3\text{O}_4$  and  $\gamma\text{-Fe}_2\text{O}_3$  both have spinel crystal structure. So, the  $870 \text{ cm}^{-1}$  Raman peak could confidently be attributed to vibrations of oxo-bridge di-iron  $\text{O}-\text{Fe}-\text{O}$  bonds at the magnetite/maghemite interface. Its transient character is due to the appearance of the maghemite phase and its disappearance once the majority of the nanoparticles has changed to the hematite phase. This attribution is corroborated by the work of El Mendili et al.<sup>23</sup> who recently reported on the transition of 4 nm iron oxide nanoparticles from the maghemite phase to the hematite phase. Since there was no initial magnetite phase (and thus no magnetite/maghemite interface) in their nanoparticles, they did not observe the  $870 \text{ cm}^{-1}$  transient peak in their Raman spectra.

The presence of lepidocrocite could play a role in the magnetite to hematite phase transition. Indeed, it has been shown experimentally that the surface of  $\gamma\text{-FeOOH}$  is effective for catalytic oxidation of  $\text{Fe}(\text{II})$  which facilitates the transition of  $\text{Fe}_3\text{O}_4$  into  $\gamma\text{-Fe}_2\text{O}_3$ .<sup>49</sup> Moreover, it is well-known that  $\gamma\text{-FeOOH}$  is unstable and can easily change to  $\gamma\text{-Fe}_2\text{O}_3$  under laser irradiation<sup>40</sup> or heat treatment.<sup>50</sup> On the basis of this assumption, and on our SERS experiments, we thus propose a phase transition scheme of our  $\text{Fe}_3\text{O}_4$ -decorated AuNPs (Figure 7).

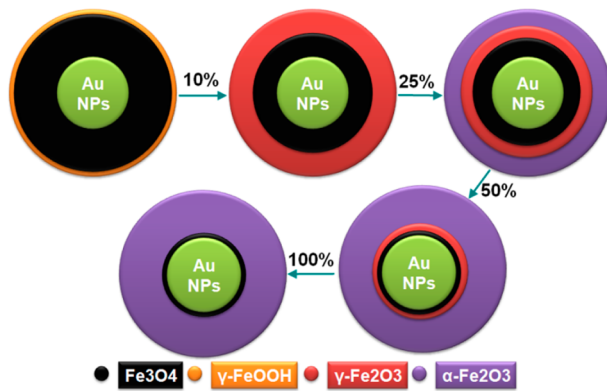


**Figure 7.** Schematic of the transition of the iron oxide shell from the magnetite ( $\text{Fe}_3\text{O}_4$ ) phase to the hematite ( $\alpha\text{-Fe}_2\text{O}_3$ ) phase under laser irradiation. The phase transition is triggered and catalyzed by the lepidocrocite ( $\gamma\text{-FeOOH}$ ) surface layer. Initially, the shell consists of lepidocrocite and magnetite. At  $1.4 \times 10^6 \text{ W cm}^{-2}$  laser intensity, the lepidocrocite oxidizes, and the maghemite ( $\gamma\text{-Fe}_2\text{O}_3$ ) phase appears. At  $3.5 \times 10^6 \text{ W cm}^{-2}$  (25%), the hematite ( $\alpha\text{-Fe}_2\text{O}_3$ ) phase comes out, increases at  $7 \times 10^6 \text{ W cm}^{-2}$  (50%), and becomes dominant at  $1.4 \times 10^7 \text{ W cm}^{-2}$  (100%). The percentages in brackets and in the figure indicate the laser intensity in percentage of the maximum value.

As shown in Figure 7, we suggest that the phase transition is triggered by the lepidocrocite surface layer which transforms to maghemite thus leading to biphasic nanoparticles in which the magnetite and maghemite phases coexist. With increasing laser intensity the maghemite phase becomes dominant and gives rise to the hematite phase at large laser intensities.

It is interesting to address the impact of the plasmonic properties of the  $\text{Fe}_3\text{O}_4$ -decorated AuNPs on their phase transition properties. To do so, we have estimated the temperature elevation due to plasmonic resonance assisted heating of the NPs. Assuming an isolated  $\text{Au}-\text{Fe}_3\text{O}_4$  nanoparticle with radius  $a$ , the temperature  $T$  at the surface of the  $\text{Fe}_3\text{O}_4$  shell is given by  $T = T_0 + (\sigma_{\text{abs}} I)/(4\pi k a)$ <sup>51</sup> where  $T_0$  is the room temperature,  $I$  the laser intensity, and  $\sigma_{\text{abs}}$  the absorption cross section at the laser excitation wavelength (638 nm);  $k = 3.8 \text{ W m}^{-1} \text{ K}^{-1}$  is the thermal conductivity of  $\text{Fe}_3\text{O}_4$ .<sup>52</sup>  $\sigma_{\text{abs}}$  is obtained from the DDA simulations. For  $I = 1.4 \times 10^5 \text{ W cm}^{-2}$  one obtains  $T = 35^\circ\text{C}$  (including  $25^\circ\text{C}$  room temperature). This temperature is well below the transition temperature of magnetite to maghemite ( $\geq 200^\circ\text{C}$ ),<sup>25</sup> and the SERS spectrum (Figure 6) shows no Raman features of maghemite, indeed. Increasing the laser intensity to  $1.4 \times 10^6 \text{ W cm}^{-2}$  gives  $T = 125^\circ\text{C}$ . The latter is still below the transition temperature of magnetite to maghemite. Nevertheless, such a transition is observed for  $1.4 \times 10^6 \text{ W cm}^{-2}$  (Figure 6). In fact, our measurements were performed on NP aggregates, and therefore the temperature elevation is due to several absorbing

particles. So, the actual temperature could be larger than the estimated 125 °C and above the magnetite to maghemite transition temperature (200 °C) but still below the transition temperature of maghemite to hematite ( $\geq 400$  °C).<sup>25</sup> The latter is reached or surpassed with  $I = 3.5 \times 10^6$  W cm<sup>-2</sup> as shown in Figure 6. The high temperature, due to laser heating, could damage the surfactant and may thus lead to a collapse of the hybrid structure. However, as can be noticed in Figure 6, the Raman peaks of maghemite and hematite produced by the phase transition of magnetite are well-defined: their line width and relative intensities are comparable to those reported for bulk materials.<sup>23–25</sup> In case of collapse, one expects a strong broadening and even a vanishing of the Raman features of the Fe<sub>3</sub>O<sub>4</sub> decoration which is not the case here.

It is worthwhile to mention that isolated Fe<sub>3</sub>O<sub>4</sub> NPs (Figure 1) have no influence on the SERS or phase transition properties. From Figure 5 one can see that the Raman scattering is strongly resonant with the surface plasmons of the Fe<sub>3</sub>O<sub>4</sub>-decorated nanoparticles. Hence, the nonresonant Raman signal of isolated Fe<sub>3</sub>O<sub>4</sub> NPs is very weak.

#### 4. CONCLUSION

In summary, we have reported the synthesis of hybrid Au–Fe<sub>3</sub>O<sub>4</sub> nanoparticles using a novel one-pot process, and have studied their plasmonic and SERS related properties as well as their phase transition properties. We found that the nanoparticles exhibit a strong plasmonic resonance that produces an intense SERS signal. The study of the temporal fluctuations of the SERS allowed us to identify the Raman scattering from the thin Fe<sub>3</sub>O<sub>4</sub> shell. By combining SERS experiments and numerical simulations of the plasmonic near fields, we were able to investigate the fine structure of the Fe<sub>3</sub>O<sub>4</sub> shell and to point out the presence of an iron hydroxide layer that plays an important role in the phase transition properties of the hybrid nanoparticles. By changing the laser intensity, we have investigated the transformation of the magnetite Fe<sub>3</sub>O<sub>4</sub> shell into maghemite and hematite. We have reported the observation of Raman scattering by di-iron oxobridge bonds associated with the intermediate magnetite/maghemite mixed state. The observation of such fine details was possible owing to the strong plasmonic resonance carried by the Au cores. Further efforts will be paid to the control of the size and the structure of the Fe<sub>3</sub>O<sub>4</sub> shell and to the investigation of the magneto-plasmonic properties of these hybrid Au–Fe<sub>3</sub>O<sub>4</sub> nanoparticles.

Finally, we would like to comment on the consequences of our work on possible applications of Au–Fe<sub>3</sub>O<sub>4</sub> nanoparticles.

First, it is well-known that iron oxides (magnetite and hematite) have a good photocatalytic activity.<sup>53,54</sup> Their combination with gold nanoparticles is very interesting because the photocatalysis process may be enhanced using plasmonic resonances.<sup>55–57</sup> Our results clearly show that the plasmonic field in our Fe<sub>3</sub>O<sub>4</sub>-decorated AuNPs is concentrated in the Fe<sub>3</sub>O<sub>4</sub> shell which is necessary for efficient generation of electrons and holes. In addition, the shell thickness is only a few nanometers which is a short distance for electrons and holes to reach the nanoparticle surface and give rise to redox reactions in the solvent.

Second, applications of hybrid Au–Fe<sub>3</sub>O<sub>4</sub> nanoparticles based on their optical properties rely on the possibility of combining plasmonic and magnetic excitations. For instance, it is well-known that magnetic hysteresis leads to heating of the nanoparticle.<sup>58</sup> On the other hand, plasmonic resonance can be

exploited for converting electromagnetic energy into heat.<sup>59</sup> So, combining these two heat generation sources within a single hybrid nanoparticle may pave the way to efficient cancer therapy based on the hyperthermia effect. Therefore, it is important to investigate the behavior of the hybrid Au–Fe<sub>3</sub>O<sub>4</sub> nanoparticles upon laser irradiation. Our results show that the synthesized Fe<sub>3</sub>O<sub>4</sub>-decorated AuNPs are robust: the transition from the magnetite to the hematite phase (with a loss of magnetic properties) occurs at irradiation intensity around  $1.4 \times 10^6$  W/cm<sup>2</sup> which is much larger than the intensity (few tens of watts/cm<sup>2</sup>) usually used in hyperthermia experiments on live tissues.<sup>59</sup>

#### ■ ASSOCIATED CONTENT

##### S Supporting Information

(i) Synthesis mechanism of Au–Fe<sub>3</sub>O<sub>4</sub> in the presence of sodium citrate, (ii) table containing the assignment of the Raman bands, (iii) calculated optical extinction spectra of Au–Fe<sub>3</sub>O<sub>4</sub> dimers, and (iv) two video clips showing the temporal fluctuations of the signal excited at 638 and 785 nm. This material is available free of charge via the Internet at <http://pubs.acs.org>.

#### ■ AUTHOR INFORMATION

##### Corresponding Author

\*E-mail: aden.mlayah@cemes.fr. Tel.: +33 05 62 25 78 36.

##### Notes

The authors declare no competing financial interest.

#### ■ ACKNOWLEDGMENTS

Amine Mezni gratefully acknowledges support by the ministry of higher education and scientific research of Tunisia. This work was supported by the CALMIP high performance computing facilities at Paul Sabatier University of Toulouse.

#### ■ REFERENCES

- (1) Choi, S. H.; Na, H. B.; Park, Y. I.; An, K.; Kwon, S. G.; Jang, Y.; Park, M.; Moon, J.; Son, J. S.; Song, I. C.; et al. Simple and Generalized Synthesis of Oxide-Metal Heterostructured Nanoparticles and Their Applications in Multimodal Biomedical Probes. *J. Am. Chem. Soc.* **2008**, *130*, 15573–15580.
- (2) Yu, T.; Zeng, J.; Lim, B.; Xia, Y. N. Aqueous-Phase Synthesis of Pt/CeO<sub>2</sub> Hybrid Nanostructures and Their Catalytic Properties. *Adv. Mater.* **2010**, *22*, 5188–5192.
- (3) Bang, J. H.; Kamat, P. V. Quantum Dot Sensitized Solar Cells. A Tale of Two Semiconductor Nanocrystals: CdSe and CdTe. *ACS Nano* **2009**, *3*, 1467–1476.
- (4) Thomann, I.; Pinaud, B. A.; Chen, Z.; Clemens, B. M.; Jaramillo, T. F.; Brongersma, M. L. Plasmon Enhanced Solar-to-Fuel Energy Conversion. *Nano Lett.* **2011**, *11*, 3440–3446.
- (5) Zhang, J. T.; Tang, Y.; Lee, K.; Ouyang, M. Tailoring Light-Matter-Spin Interactions in Colloidal Hetero-Nanostructures. *Nature* **2010**, *466*, 91–95.
- (6) Chaudhuri, R. G.; Paria, S. Core/Shell Nanoparticles: Classes, Properties, Synthesis Mechanisms, Characterization, and Applications. *Chem. Rev.* **2012**, *112*, 2373–2433.
- (7) Shi, W.; Zeng, H.; Sahoo, Y.; Ohulchansky, T. Y.; Ding, Y.; Wang, Z. L.; Swihart, M.; Prasad, P. N. A General Approach to Binary and Ternary Hybrid Nanocrystals. *Nano Lett.* **2006**, *6*, 875–881.
- (8) Xie, J.; Zhang, F.; Aronova, M.; Zhu, L.; Lin, X.; Quan, Q.; Liu, G.; Zhang, G.; Choi, K.-Y.; Kim, K.; et al. Manipulating the Power of an Additional Phase: A Flower-like Au–Fe<sub>3</sub>O<sub>4</sub> Optical Nanosensor for Imaging Protease Expressions in Vivo. *ACS Nano* **2011**, *5*, 3043–3051.

- (9) Leung, K. C.-F.; Xuan, S.; Zhu, X.; Wang, D.; Siu-Fung Lee, C.-P. C.; Hob, W. K.-W.; Chung, B. C.-T. Gold and Iron Oxide Hybrid Nanocomposite Materials. *Chem. Soc. Rev.* **2012**, *41*, 1911–1928.
- (10) Kim, J.; Park, S.; Lee, J. E.; Jin, S. M.; Lee, J. H.; Lee, I. S.; Yang, I.; Kim, J.-S.; Kim, S. K.; Cho, M.-H.; Hyeon, T. Designed Fabrication of Multifunctional Magnetic Gold Nanoshells and Their Application to Magnetic Resonance Imaging and Photothermal Therapy. *Angew. Chem., Int. Ed.* **2006**, *45*, 7754–7758.
- (11) Brullot, W., MSC; Valev, V. K.; Verbiest, T. Magnetic-Plasmonic Nanoparticles for the Life Sciences: Calculated Optical Properties of Hybrid Structures. *Nanomed.-Nanotechnol. Biol., Med.* **2012**, *8*, 559–568.
- (12) Song, H.-M.; Wei, Q. S.; Ong, Q. K.; Wei, A. Plasmon-Resonant Nanoparticles and Nanostars with Magnetic Cores: Synthesis and Magnetomotive Imaging. *ACS Nano* **2010**, *4*, 5163–5173.
- (13) Gu, H. W.; Xu, K. M.; Xu, C. J.; Xu, B. Biofunctional Magnetic Nanoparticles for Protein Separation and Pathogen Detection. *Chem. Commun.* **2006**, *46*, 941–949.
- (14) Bao, J.; Chen, W.; Liu, T. T.; Zhu, Y. L.; Jin, P. Y.; Wang, L. Y.; Liu, J. F.; Wei, Y. G.; Li, Y. D. Bifunctional Au-Fe<sub>3</sub>O<sub>4</sub> Nanoparticles for Protein Separation. *ACS Nano* **2007**, *1*, 293–298.
- (15) Kumari, S.; Singh, R. P. Glycolic Acid Functionalized. *Int. J. Biol. Macromol.* **2013**, *54*, 244–249.
- (16) Peng, H.-P.; Liang, R.-P.; Zhang, L.; Qiu, J.-D. Facile Preparation of Novel Core Shell Enzyme-Au-Polydopamine-Fe<sub>3</sub>O<sub>4</sub> Magnetic Bionanoparticles for Glucose Sensor. *Biosens. Bioelectron.* **2013**, *42*, 293–299.
- (17) Shi, W. L.; Zeng, H.; Sahoo, Y.; Ohulchanskyy, T. Y.; Ding, Y.; Wang, Z. L.; Swihart, M.; Prasad, P. N. A General Approach to Binary and Ternary Hybrid Nanocrystals. *Nano Lett.* **2006**, *6*, 875–881.
- (18) Wei, Y. H.; Klajn, R.; Pinchuk, A. O.; Grzybowski, B. A. Synthesis, Shape Control, and Optical Properties of Hybrid Au/Fe<sub>3</sub>O<sub>4</sub> “Nanoflowers”. *Small* **2008**, *4*, 1635–1639.
- (19) Sheng, Y.; Xue, J. Synthesis and Properties of Au-Fe<sub>3</sub>O<sub>4</sub> Heterostructured Nanoparticles. *J. Colloid Interface Sci.* **2012**, *374*, 96–101.
- (20) Bao, J.; Chen, W.; Liu, T. T.; Zhu, Y. L.; Jin, P. Y.; Wang, L. Y.; Liu, J. F.; Wei, Y. G.; Li, Y. D. Bifunctional Au-Fe<sub>3</sub>O<sub>4</sub> Nanoparticles for Protein Separation. *ACS Nano* **2007**, *1*, 293–298.
- (21) Chao Wang, Y. W.; Jiang, H.; Sun, S. Tug-of-War in Nanoparticles: Competitive Growth of Au on Au-Fe<sub>3</sub>O<sub>4</sub> Nanoparticles. *Nano Lett.* **2009**, *9*, 4544–4547.
- (22) Liu, H. L.; Wu, J. H.; Min, J. H.; Kim, Y. K. One-Pot Synthesis and Characterization of Bifunctional Au-Fe<sub>3</sub>O<sub>4</sub> Hybrid Core–Shell Nanoparticles. *J. Alloys Compd.* **2012**, *537*, 60–64.
- (23) Mendili, Y. E.; Bardeau, J.-F.; Randrianantoandro, N.; Grasset, F.; Geneche, J.-M. Insights Into the Mechanism Related to the Phase Transition from  $\gamma$ -Fe<sub>2</sub>O<sub>3</sub> to  $\alpha$ -Fe<sub>2</sub>O<sub>3</sub> Nanoparticles Induced by Thermal Treatment and Laser Irradiation. *J. Phys. Chem. C* **2012**, *116*, 23785–23792.
- (24) Guo, C.; Hu, Y.; Qian, H.; Ning, J.; Xu, S. Magnetite (Fe<sub>3</sub>O<sub>4</sub>) Tetrahexahedral Microcrystals: Synthesis, Characterization, and Micro-Raman Study. *Mater. Charact.* **2011**, *62*, 148–151.
- (25) Jubb, A. M.; Allen, H. C. Vibrational Spectroscopic Characterization of Hematite, Maghemite, and Magnetite Thin Films Produced by Vapor Deposition. *ACS Appl. Mater. Interfaces* **2010**, *2*, 2804–2812.
- (26) Draine, B. T.; Flatau, P. J. The Discrete Dipole Approximation for Periodic Targets: I. Theory and Tests. *J. Opt. Soc. Am. A* **1994**, *11*, 1491–1499.
- (27) Draine, B. T.; Flatau, P. J. User Guide to the Discrete Dipole Approximation Code DDSCAT 7.2, 2012, <http://arXiv.org/abs/1202.3424>.
- (28) Johnson, P. B.; Christy, R. W. Optical Constants of the Noble Metals. *Phys. Rev. B* **1972**, *6*, 4370–4379.
- (29) Schlegel, A.; Alvarado, S. F.; Wachter, P. Optical Properties of Magnetite (Fe<sub>3</sub>O<sub>4</sub>). *J. Phys. C: Solid State Phys.* **1979**, *12*, 1157–1164.
- (30) Poul, L.; Jouini, N.; Fievet, F. Layered Hydroxide Metal Acetates (Metal = Zinc, Cobalt, and Nickel): Elaboration via Hydrolysis in Polyol Medium and Comparative Study. *Chem. Mater.* **2000**, *12*, 3123–3132.
- (31) Livage, J.; Henry, M.; Sanchez, C. Sol-Gel Chemistry of Transition Metal Oxides. *Prog. Solid State Chem.* **1988**, *18*, 250–341.
- (32) Fievet, F.; Lagier, J. P.; Blin, B. Homogeneous and Heterogeneous Nucleations in the Polyol Process for the Preparation of Micro and Submicron Size Metal Particles. *Solid State Ionics* **1989**, *32/33*, 198–205.
- (33) Jeonb, M.; Moona, J.; Ji, X.; Song, X.; Li, J.; Bai, Y.; Yang, W.; Peng, X. Size Control of Gold Nanocrystals in Citrate Reduction: The Third Role of Citrate. *J. Am. Chem. Soc.* **2007**, *129*, 13939–13948.
- (34) Shevchenko, E. V.; Bodnarchuk, M. I.; Kovalenko, M. V.; Talapin, D. V.; Smith, R. K.; Aloni, S.; Heiss, W.; Alivisatos, A. P. Gold/Iron Oxide Core/Hollow-Shell Nanoparticles. *Adv. Mater.* **2008**, *20*, 4323–4329.
- (35) Flatau, P. J.; Draine, B. T. Fast Near-Field Calculations in the Discrete Dipole Approximation for Regular Rectilinear Grids. *Opt. Express* **2012**, *20*, 1247–1252.
- (36) Itoh, T.; Iga, M.; Tamaru, H.; Yoshida, K.-I.; Biju, V.; et al. Quantitative Evaluation of Blinking in Surface Enhanced Resonance Raman Scattering and Fluorescence by Electromagnetic Mechanism. *J. Chem. Phys.* **2012**, *136*, 1–8.
- (37) Nie, S.; Emory, S. R. Probing Single Molecules and Single Nanoparticles by Surface-Enhanced Raman Scattering. *Science* **1997**, *275*, 1102–1106.
- (38) Emory, S. R.; Jensen, R. A.; Wenda, T.; Han, M. Y.; Nie, S. Re-examining the Origins of Spectral Blinking in Single-Molecule and Single-Nanoparticle SERS. *Faraday Discuss.* **2006**, *132*, 249–259.
- (39) Lombardi, J. R.; Birke, R. L. Single Molecule SERS Spectral Blinking and Vibronic Coupling. *J. Phys. Chem. C* **2011**, *115*, 4540–4545.
- (40) Thibeau, R. J.; Brown, C. W.; Heidersbach, R. H. Raman Spectra of Possible Corrosion Products of Iron. *Appl. Spectrosc.* **1978**, *32*, 532–535.
- (41) Shebanova, O. N.; Lazor, P. Raman Study of Magnetite (Fe<sub>3</sub>O<sub>4</sub>): Laser-Induced Thermal Effects and Oxidation. *J. Raman Spectrosc.* **2003**, *34*, 845–852.
- (42) Shebanova, O. N.; Lazor, P. Raman Spectroscopic Study of Magnetite (FeFe<sub>2</sub>O<sub>4</sub>): a New Assignment for the Vibrational Spectrum. *J. Solid State Chem.* **2003**, *174*, 424–430.
- (43) de Faria, D. L. A.; Venancio Silva, S.; de Oliveira, M. T. Microspectroscopy of Some Iron Oxides Raman and Oxyhydroxides. *L. J. Raman Spectrosc.* **1997**, *28*, 873–878.
- (44) Romero, I.; Aizpurua, J.; Bryant, G. W.; Javier García de Abajo, F. Plasmons in Nearly Touching Metallic Nanoparticles: Singular Response in the Limit of Touching Dimmers. *Opt. Express* **2006**, *11*, 1–12.
- (45) Nordlander, P.; Oubre, C. Plasmon Hybridization in Nanoparticle Dimers. *Nano Lett.* **2004**, *4*, 899–903.
- (46) Ye, E.; Win, K. Y.; Tan, H. R.; Lin, M.; Teng, C. P.; Mlayah, A.; Han, M.-Y. Plasmonic Gold Nanocrosses with Multidirectional Excitation and Strong Photothermal Effect. *J. Am. Chem. Soc.* **2011**, *133*, 8506–8509.
- (47) Gallagher, J.; Feitknecht, W.; Mannweiler, U. Mechanism of Oxidation of Magnetite to  $\gamma$ -Fe<sub>2</sub>O<sub>3</sub>. *Nature* **1968**, *217*, 1118–1121.
- (48) Kurtz, D. M., Jr. Oxo- and Hydroxo-Bridged Diiron Complexes: A Chemical Perspective on a Biological Unit. *Chem. Rev.* **1990**, *90*, 585–606.
- (49) Sung, W. *Catalytic Effects of the  $\gamma$ -FeOOH (lepidocrocite) Surface on the Oxygenation Removal Kinetics of Fe(II) and Mn(II)*; California Institute of Technology: Pasadena, CA, 1980.
- (50) Gehring, A. U.; Hofmeister, A. M. The Transformation of Lepidocrocite During Heating a Magnetic and Spectroscopic Study. *Clays Clay Miner.* **1994**, *42*, 409–415.
- (51) Baffou, G.; Girard, C.; Quillard, R. Mapping Heat Origin in Plasmonic Structures. *Phys. Rev. Lett.* **2010**, *104*, 136805–136808.
- (52) Mølgård, J.; Smeltzer, W. W. Thermal Conductivity of Magnetite and Hematite. *J. Appl. Phys.* **1971**, *42*, 3644–3647.

- (53) Thimsen, E.; Formal, F. L.; Gratzel, M.; Warren, S. C. Influence of Plasmonic Au Nanoparticles on the Photoactivity of  $\text{Fe}_2\text{O}_3$  Electrodes for Water Splitting. *Nano Lett.* **2011**, *11*, 35–43.
- (54) Thomann, I.; Pinaud, B. A.; Chen, Z.; Clemens, B. M.; Jaramillo, T. F.; Brongersma, M. L. Plasmon Enhanced Solar-to-Fuel Energy Conversion. *Nano Lett.* **2011**, *11*, 3440–3446.
- (55) Qurashi, A.; Zhong, Z.; Alam, M. W. Synthesis and Photocatalytic Properties of  $\alpha\text{-Fe}_2\text{O}_3$  Nanoellipsoids. *Solid State Sci.* **2010**, *12*, 1516–1519.
- (56) Han, L.; Chenb, Y.; We, Y. Hierarchical Flower-Like  $\text{Fe}_3\text{O}_4$  and  $\gamma\text{-Fe}_2\text{O}_3$  Nanostructures: Synthesis, Growth Mechanism and Photocatalytic Properties. *Cryst. Eng. Comm.* **2012**, *14*, 4692–4698.
- (57) Gao, H.; Liu, C.; Jeong, H. E.; Yang, P. Plasmon-Enhanced Photocatalytic Activity of Iron Oxide on Gold Nanopillars. *Nano Lett.* **2012**, *6*, 234–240.
- (58) Pankhurst, Q. A.; Connolly, J.; Jones, S. K.; Dobson, J. Applications of Magnetic Nanoparticles in Biomedicine. *J. Phys. D: Appl. Phys.* **2003**, *36*, R167–R181.
- (59) Jain, P. K.; El-Sayed, I. H.; El-Sayed, M. A. Au Nanoparticles Target Cancer. *Nano Today* **2007**, *2*, 1–18.